RESEARCH ARTICLE SUMMARY

HUMAN GENOMICS

The origins and functional effects of postzygotic mutations throughout the human life span

Nicole B. Rockweiler*, Avinash Ramu, Liina Nagirnaja, Wing H. Wong, Michiel J. Noordam, Casey W. Drubin, Ni Huang, Brian Miller, Ellen Z. Todres, Katinka A. Vigh-Conrad, Antonino Zito, Kerrin S. Small, Kristin G. Ardlie, Barak A. Cohen, Donald F. Conrad*

INTRODUCTION: Mutation lays the foundation for genetics, evolution, and our very existence and demise. Historically, genetics has focused on inherited variants and has only recently begun to examine the genetic changes that occur after fertilization, known as postzygotic mutations (PZMs). This bias is partially because of technological limitations and the simplifying assumption that all cells in a multicellular organism share the same genome.

RATIONALE: Most PZM research has been single-tissue studies. An exciting next generation of PZM studies now examine PZMs across multiple tissues within an individual. However, the relatively small number of individuals and tissue types examined thus far have limited the ability to ascribe sources of mutation variation among individuals or to provide detailed descriptions of embryonic mutations that occur after the first few cell divisions.

RESULTS: To expand the field's knowledge of the origins and functional consequences of PZMs, we sought to answer four key questions: (i) Are PZMs detectable? (ii) Where do PZMs occur? (iii) When do PZMs occur? (iv) When do PZMs contribute to phenotypic variation?

We developed a suite of methods called Lachesis to detect single-nucleotide DNA PZMs from bulk RNA sequencing (RNA-seq) data. We applied these methods to the final major release of the NIH Genotype-Tissue Expression (GTEx) project—a catalog of 17,382 samples derived from 948 donors across 54 diverse tissues and cell types—to generate one of the largest and most diverse catalogs of PZMs in normal individuals.

PZMs were pervasive and highly variable among donors and tissues. Nearly half of the variation in mutation burden among tissue samples was explained by technical and biological effects, such as age and tissue type. We also found that 9% of this variation was attributed to donor-specific effects. This means that there may be systematic differences among individuals in the number of mutations that they carry due to genetic and/or environmental effects, even after controlling for age. The types of mutations, i.e., mutation spectra, were also variable across tissues, which suggests that mutational mechanisms may be different across tissues.

To estimate when PZMs occur during development, we first identified putative prenatal PZMs in the catalog and then mapped them to a developmental tree. Mutation burden and spectra varied throughout prenatal development, with early embryogenesis being the most mutagenic.

Finally, to investigate the functional consequences of PZMs, we compared the predicted deleteriousness and selection strength on PZMs across space and time. We found that the predicted functional impact of PZMs varies during prenatal development and across tissues, and we identified a class of low-frequency prenatal mutations apparently more deleterious than all other forms of human genetic variation considered. The deleteriousness of germline mutations decreased through the lifecycle: testicular germ cells carried more deleterious mutations than ejaculated sperm and sperm resulting in viable offspring.

CONCLUSION: In this work, we present methods for detecting PZMs and a comprehensive and diverse atlas of PZMs in normal development and aging. Akin to how expansive surveys of normal germline variation are immensely beneficial for human and medical genetics, this catalog contributes to our understanding of normal postzygotic variation so that abnormal variation can be identified and interpreted. Uncovering the effects of these PZMs on human health and disease is an exciting and valuable endeavor. ■

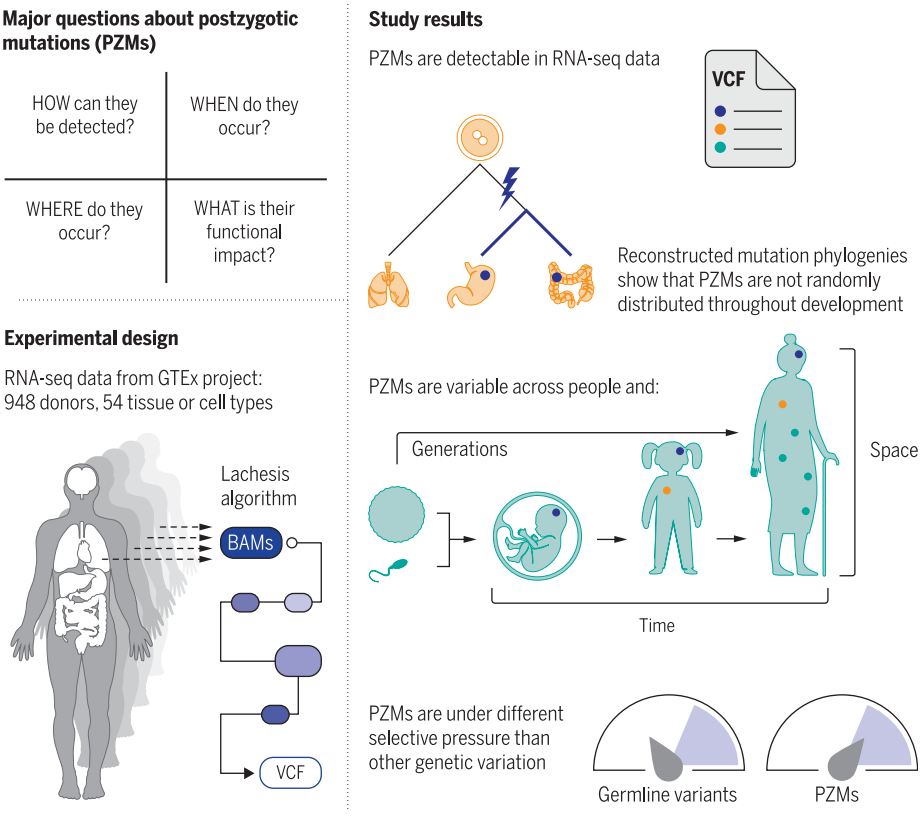

Postzygotic DNA mutations accumulate in the human body, are copied into RNA, and are detected by RNA-seq. A developmental map of these mutations resolves when and where in the body they occur and finds that the selection pressure on PZMs is different from inherited germline variants. BAMs, binary alignment maps; VCF, variant call format.

The list of author affiliations is available in the full article online.
*Corresponding author. Email: nrockweiler@wustl.edu (N.B.R.); conradon@ohsu.edu (D.F.C.)
Cite this article as N. B. Rockweiler *et al.*, *Science* **380**, eabn7113 (2023). DOI: 10.1126/science.abn7113

READ THE FULL ARTICLE AT
https://doi.org/10.1126/science.abn7113

RESEARCH ARTICLE

HUMAN GENOMICS

The origins and functional effects of postzygotic mutations throughout the human life span

Nicole B. Rockweiler[1]*†, Avinash Ramu[1], Liina Nagirnaja[2], Wing H. Wong[3]‡, Michiel J. Noordam[1], Casey W. Drubin[1], Ni Huang[1]§, Brian Miller[2], Ellen Z. Todres[4], Katinka A. Vigh-Conrad[2], Antonino Zito[5]¶, Kerrin S. Small[5], Kristin G. Ardlie[4], Barak A. Cohen[1], Donald F. Conrad[1,2,6]*

Postzygotic mutations (PZMs) begin to accrue in the human genome immediately after fertilization, but how and when PZMs affect development and lifetime health remain unclear. To study the origins and functional consequences of PZMs, we generated a multitissue atlas of PZMs spanning 54 tissue and cell types from 948 donors. Nearly half the variation in mutation burden among tissue samples can be explained by measured technical and biological effects, and 9% can be attributed to donor-specific effects. Through phylogenetic reconstruction of PZMs, we found that their type and predicted functional impact vary during prenatal development, across tissues, and through the germ cell life cycle. Thus, methods for interpreting effects across the body and the life span are needed to fully understand the consequences of genetic variants.

The effects of age ravage all tissues of the body, but the pace and consequences of age-related decay vary among tissues and people. The accumulation of DNA damage is thought to be a primary agent of age-related disease (*1*), and surveys of postzygotic mutations (PZMs) in normal tissues [for example, blood (*2*–*4*), brain (*5*), and skin (*6*, *7*)] and across the body (*8*–*10*) have found PZMs to be pervasive across the genome and individuals. However, beyond cancer, there are few conditions where PZMs are known to have a causal role. Because of the high cost and technological challenges of PZM studies, a general understanding of how and when mutation affects the function of specific cell and tissue types is essential for defining research priorities. One way to prioritize hypotheses about mutation and disease is to systematically characterize the consequences of PZMs on cellular fitness across a broad range of tissues. Surveys of normal tissues have found that PZMs appear to accrue neutrally (*10*, *11*), but positive and negative selection do occur in specific genes and cellular contexts, which suggests that PZMs affect cellular function.

Another fundamental question is how the timing of mutation modulates risk for diseases. As clearly demonstrated in oncology, it is possible to detect disease-causing PZMs and augment clinical care years before clinical disease is recognized (*12*, *13*). If PZMs that confer risk for disease accrue across the life span, the PZM profile in a healthy individual could contain actionable prognostic information. Although the relative contributions of prenatal and postnatal PZMs to disease risk are unclear, because of the massive cell proliferation during development, prenatal PZMs have the potential to affect many cells and, thus, to play an important role in disease.

Most PZM research has been single-tissue studies largely focused on tissues that are easily accessible, such as blood, liver, skin, and colon. An exciting next generation of PZM studies now examines PZMs across multiple tissues within an individual (*8*–*10*, *14*). However, the relatively small numbers of individuals and tissue types used in such studies have limited the ability to ascribe sources of mutation variation among individuals or to provide detailed descriptions of embryonic mutations that occur after the first few cell divisions. To expand our knowledge of PZMs in normal tissues, we developed a suite of methods called Lachesis to identify single-nucleotide PZMs from bulk RNA sequencing (RNA-seq) data and predict when the mutations occurred during development and aging (figs. S1 and S2). We ran the algorithm on the final major release of the Genotype Tissue Expression project (GTEx)—a collection of RNA-seq data from 17,382 samples derived from 948 donors across 54 diverse tissues and cell types—to generate one of the most comprehensive databases of PZMs in normal tissues (*15*, *16*) (tables S1 to S8). We used this atlas and the rich metadata on GTEx donors to characterize sources of variation in PZM burden among individuals and unveil the spatial, temporal, and functional variation of PZMs in normal development and aging.

DNA PZMs are accurately detected in bulk tissue RNA-seq

We evaluated the accuracy of the algorithm using several in silico and experimental methods (figs. S3 and S4 and tables S3 to S6). For experimental validation, we obtained four independent DNA- and RNA-based validation datasets generated from the same tissue samples as the primary data covering 296 specific genomic sites across 95 samples. The original PZM variant allele frequency (VAF) estimates from RNA-seq were well correlated with the VAFs from DNA-seq (Spearman's $\rho = 0.82$, P value $= 2.3 \times 10^{-25}$), which suggests that RNA-seq–based VAFs are representative of true mutant cell frequencies. PZMs with VAFs as low as 0.16% and PZMs found in multiple tissues and multiple donors were validated. The average false discovery rate (FDR) across all validation datasets was 27% and was lower than with published methods for detecting PZMs from RNA-seq (34 to 82%) (*8*, *9*, *17*) (fig. S1E and table S3). Because mutations may fail to validate as a result of spatial variation in mosaicism, the FDRs may be overestimated. A small subset of samples (~5%) had an extraordinarily high number of detected PZMs; validation data from these samples produced an average FDR estimate of 98% (table S3). We conclude that these outliers were likely technical artifacts and not hypermutated tissues.

We used power simulations to estimate the algorithm's sensitivity. As expected, simulated PZMs with larger VAFs and higher coverage had higher PZM detection power. At the middle quintile of coverage [(673, 1395) fold coverage), PZMs with VAFs as low as 0.66% could be detected in at least 90% of simulations, which suggests that the method has reasonable sensitivity (fig. S1F).

PZMs are pervasive and highly variable among donors and tissues

After sample and PZM quality control, 56,585 PZMs were detected with VAFs as low as 0.04% and a median VAF of 0.5% (table S7). These mutations are not a random sample of PZMs from the genome but a critically important subset located in the so-called allowable transcriptome—a filtered set of transcribed positions based on GENCODE 26 gene models (*16*) (table S1). In total, 100% of the donors and 77% of the tissue samples had detectable

[1]Department of Genetics, Washington University School of Medicine, St. Louis, MO 63110, USA. [2]Division of Genetics, Oregon National Primate Research Center, Oregon Health & Science University, Beaverton, OR 97006, USA. [3]Department of Pediatrics, Division of Hematology and Oncology, Washington University School of Medicine, St. Louis, MO 63110, USA. [4]Broad Institute of MIT and Harvard, Cambridge, MA 02142, USA. [5]Department of Twin Research and Genetic Epidemiology, King's College London, London SE1 7EH, UK. [6]Center for Embryonic Cell and Gene Therapy, Oregon Health & Science University, Portland, OR 97239, USA.
***Corresponding author. Email: nrockweiler@wustl.edu (N.B.R.); conradon@ohsu.edu (D.F.C.)**
†Present address: Program in Medical and Population Genetics and Stanley Center for Psychiatric Research, Broad Institute of MIT and Harvard, Cambridge, MA 02142, USA.
‡Present address: Departments of Genetics and Medicine, Stanford University, CA 94305, USA.
§Present address: T-Therapeutics Ltd., Cambridge CB21 6AD, UK.
¶Present address: Department of Molecular Biology, Massachusetts General Hospital, Boston, MA 02114, USA.

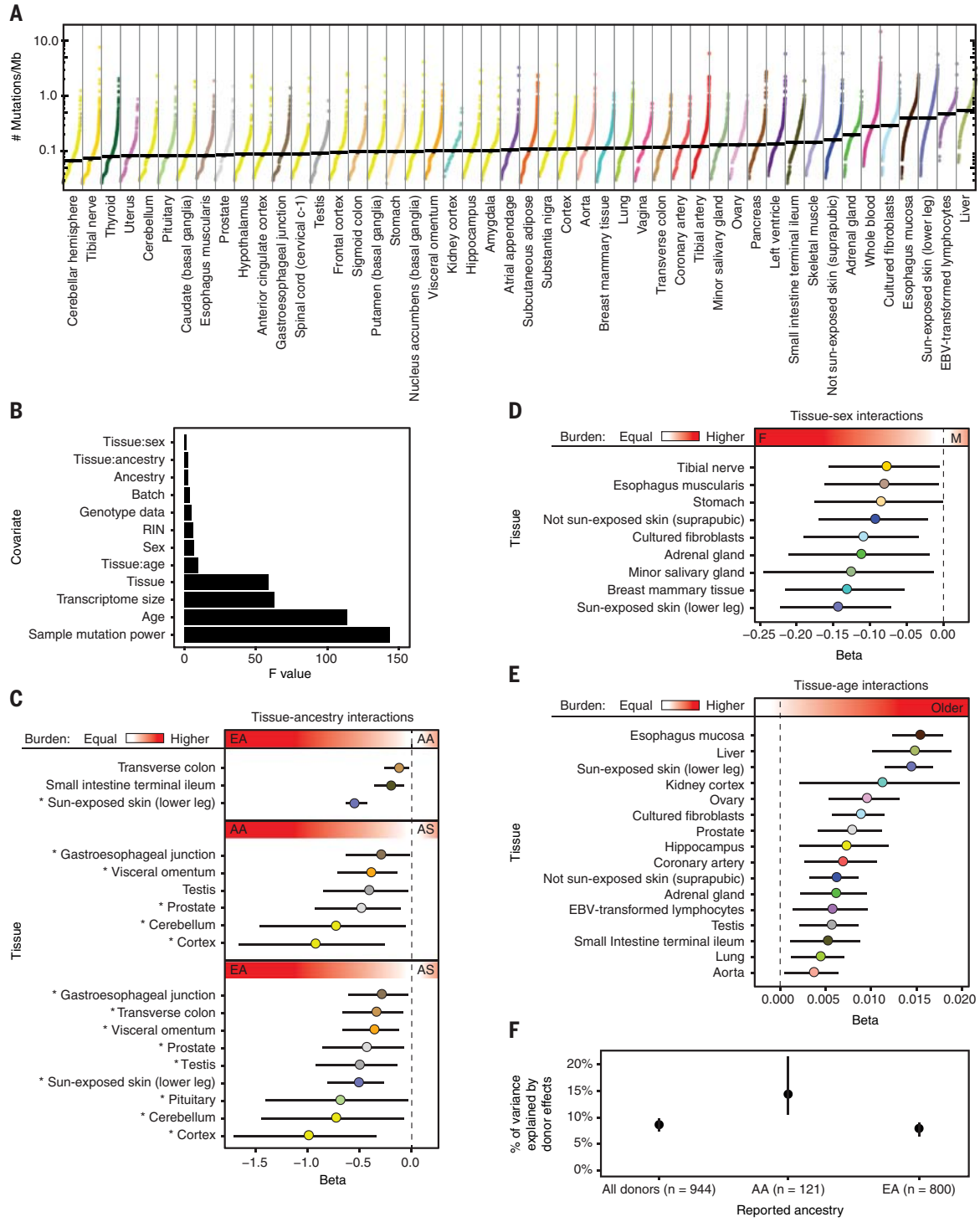

Fig. 1. PZM burden is correlated with biological and technical variables. (**A**) Each data point represents a single tissue sample and is colored by tissue. Median normalized PZM burden in a tissue denoted by the horizontal black line. Tissues are sorted by increasing median normalized PZM burden. A pseudocount of one mutation was added to each sample before normalization and log transformation for visualization. (**B**) We fit a regression model for single-tissue PZM burden using 12 covariates and 48 tissues. Shown here are the type II ANOVA F statistics for each covariate in the model. Larger F statistics correspond to greater explanatory power of the covariate. (**C** and **D**) Regression coefficients of tissue-ancestry interactions (C) and tissue-sex interactions (D) indicate strong effects of ancestry and sex on PZM burden. AA, African American; AS, Asian American; EA, European American. The asterisks in (C) denote differences in mutation burden among ancestry groups that are consistent with cancer incidence trends (*18*). (**E**) Significant positive tissue-age interaction effects were detected for 16/48 (33%) tissues. In (C) to (E), the red gradient and text labels within indicate the meaning of the regression coefficients' sign and magnitude. (**F**) Variance component estimates of donor-specific random effects on PZM burden indicate that 8 to 15% of variation among tissues can be ascribed to donor effects, which could be genetic and environmental. Dashed vertical lines at beta = 0 in interaction plots denote no association between mutation burden and interaction. [(C), (D), (E), and (F)] Error bars represent 95% CIs. [(A), (C), (D), and (E)] Tissues are colored using the GTEx coloring convention (see table S8 for a complete legend).

mosaicism (table S2). We defined the mutation burden of a sample as the number of PZMs detected in a sample and the normalized mutation burden of a sample as the mutation burden normalized by the size of the sample's transcriptome (the number of megabases with at least 20× total coverage). The median normalized mutation burden in a tissue ranged from 0.03 PZMs per expressed megabase in the cerebellar hemisphere to 0.47 PZMs per expressed megabase in the liver (Fig. 1A and table S8). The observed normalized mutation burden was more variable within a tissue than between tissues [mean median absolute deviation (MAD) within a tissue = 0.07 PZMs per expressed megabase; MAD across tissues = 0.02 PZMs per expressed megabase]. This observation suggests that processes generating detectable PZMs may be more variable across donors than across tissue types.

To build further support for the validity of our per-tissue estimates of mutation burden, we compared our data with a recent multitissue survey of PZMs based on DNA-seq of three donors (*10*, *14*). Encouragingly, when comparing 12 tissues assessed by both studies, we found reasonably high correlation in estimated PZM burden (*16*) (fig. S5). The Pearson correlation for the average burden was 0.8 ($P = 0.0018$, Pearson's correlation test).

PZM burden is correlated with biological and technical variables

To partition and quantify potential sources of single-tissue PZM burden, we fit linear models relating technical and biological metadata to single-tissue PZM burdens and selected the best fitting model identified from detailed model comparisons (*16*). The final model contained 12 covariates and explained 48% of the variation in mutation burden. All covariates yielded F test $P < 0.05$ in a type II analysis of variance (ANOVA) and included both biological (age; tissue; and interactions of tissue with age, sex, and self-reported ancestry) and technical (for example, mutation detection power and RNA extraction batch) sources of variation (Fig. 1B and table S9). In total, 20.8% (10/48) of tissues showed significant (Wald test Q value < 0.05) associations with self-reported ancestry, including, as expected, a much lower burden of mutation in sun-exposed skin in African Americans and Asian Americans compared with European Americans (*8*). The incidence rates of cancer types affecting these tissues have ancestry associations that are consistent with (in the same direction as) the mutation burden associations in 83% (15/18) of comparisons (*18*), which suggests that variation in PZM burden in normal tissues may contribute to differences in cancer risk among ancestries (Fig. 1C and table S10). Unexpectedly, males had lower burden in all three skin-related sample types compared with females (Fig. 1D). This result was essentially unchanged when removing genes inferred to have sex-biased expression (fig. S6). Age was positively associated with 33% (16/48) of tissues and was the strongest for esophagus mucosa, liver, and sun-exposed skin (Fig. 1E). We note that power may have been too low to detect some associations; for example, there were few young GTEx brain donors.

Extending this model to include a random donor effect, we estimated that 8.8% of variation in PZM burden can be attributed to systematic properties of donors that extend across some or all tissues of a donor, even after controlling for metadata such as age and sex. This donor variance component estimate was larger in African Americans [14.1%; 95% confidence interval (CI): 10.5 to 21.5%] than in European Americans (8%; 95% CI: 6.5 to 9.1%) (Fig. 1F). These unexplained donor-specific effects could have both genetic and environmental bases. Notably, a recent study estimated that 5.2% of variance in germline mutation rate could be attributed to family-specific effects (*19*). In total, our results indicate that variation in PZM rate among individuals is less constrained than variation in germline mutation rate and that there is considerable scope for heritable variation in observable PZM burden. The inability of the models to explain all variation implies that there are additional factors associated with detectable mutation burden and/or that stochasticity plays a major role in mosaicism (*20*, *21*). A reanalysis of the data that incorporated information on the apparent clonality of mutations produced models with similar biological conclusions and less explanatory power (*16*) (fig. S7 and table S11).

Mutation spectra are variable across tissues and reflect known biological processes

Diverse processes mutate the human genome with characteristic mutational signatures (*22*). Thus, the observed mutation spectra can provide insight on the types and relative activities of the unobserved mutation processes that occurred. We estimated the contribution of canonical mutation signatures for each tissue. Because of the relatively low number of detected mutations, mutation spectra were reliably deconstructed for only four tissues or cell types (*16*) (fig. S8). Consistent with expectations and previous studies (*3*, *6*, *7*), the mutations were resolved into mutational signatures associated with age in all tissues and ultraviolet light exposure in skin-related tissues (fig. S9).

For a higher powered, but coarser-grained analysis of mutation spectra, we assessed the frequency of the six base substitutions across all tissues (fig. S8). Mutation spectra were highly variable across tissues, which suggests that mutational mechanisms and their relative activity may vary across the human body. C > T was the most common mutation type across tissues, whereas C > G and T > A were the least common. Hierarchical clustering of the mutation types revealed two significant large clusters ($P < 1 \times 10^{-3}$, bootstrap resampling). We denoted these as cluster A (marked by depleted T > G) and cluster B (marked by elevated T > G). Cluster membership was associated with mutation burden, which suggests that the underlying mutation mechanisms may be coupled to the frequency of mutagenic events ($P = 3.8 \times 10^{-2}$, Mann-Whitney U test). Additionally, cluster B was enriched with neural ectoderm tissues compared with cluster A ($P = 7.7 \times 10^{-6}$, Fisher's exact test). These clusters could not be attributed to differences in sample processing (*16*) (fig. S10). We speculated that these clusters may reflect differences in the relative contributions of mutations acquired during prenatal development and mutations that accrue during age-related tissue renewal. To further study the properties of prenatal and postnatal PZMs, we developed methods to define the developmental origin of each PZM.

The developmental origins of prenatal PZMs

Multitissue PZMs exhibit prenatal properties

We defined a multitissue PZM as a PZM that was detected in at least two tissues from the same donor. Because the PZM burden was relatively low across tissues (Fig. 1) and PZMs are predominantly under neutral selection (*11*), we hypothesized that a multitissue PZM was the result of a single PZM that occurred in a common ancestor of the mutated tissues. Because the common ancestors of any set of GTEx tissues (excluding cell lines) occurred before the end of organogenesis, multitissue PZMs may have occurred prenatally. Consistent with this hypothesis, we found several lines of evidence suggesting that the multitissue PZMs occurred prenatally (*16*) (figs. S11 and S12). We found a significant positive correlation between VAF and the fraction of the donor's tissues that had the multitissue mutation detected (Spearman's $\rho = 0.34$; $P = 9.7 \times 10^{-56}$, Spearman's rank correlation test; fig. S11A). Controlling for technical and biological confounders, age was not significantly associated with multitissue mutation burden for most tissues but was significantly associated with single-tissue mutation burden for a large number of tissues (fig. S11, B and C). Additionally, the multitissue age regression coefficients were significantly smaller than the single-tissue age regression coefficients ($P = 0.016$, Wilcoxon signed-rank test) (fig. S11D). We denoted these multitissue mutations as prenatal PZMs, and all other mutations were called postnatal PZMs. We note that there may be an error rate associated with this classification because some mutations labeled as postnatal may have been prenatal mutations

lost in some tissues or may have been undetected in some donors because of limited samples.

PZM burden and spectra vary throughout prenatal development with most mutations occurring during early embryogenesis

To determine when and where PZMs occur in prenatal development, we developed a method called LachesisMap to map the origin of 1864 prenatal mutation events (*16*) (Fig. 2A, figs. S13 to S16, and table S12). Briefly, the method takes as input a directed rooted tree representing the developmental relationships among the tissues and a list of multitissue PZMs and maps the PZMs to the tree while accounting for differential mutation detection power across the genome, human body, and developmental tree. The algorithm outputs a list of edge weights that represent the estimated fraction of PZMs that occurred in that spatiotemporal window of development.

The mutation burdens across developmental time and space were highly variable, with edge weights ranging from 0.04 to 23%, and appeared compatible with an exponential distribution (P = 0.56, Kruskal-Wallis test). The ensemble of observed edge weights was significantly different from random ($P = 2.2 \times 10^{-308}$, multinomial goodness-of-fit test), and the majority of individual edge weights (56%, 14/25) were significantly different from random after Benjamini-Hochberg correction (permutation tests) (fig. S17). The top two edge weights, representing 41% of prenatal mutation events, were the zygote-to-gastrula transition and the ectoderm-to–neural ectoderm transition, which suggests that most detectable prenatal mutations occur during early

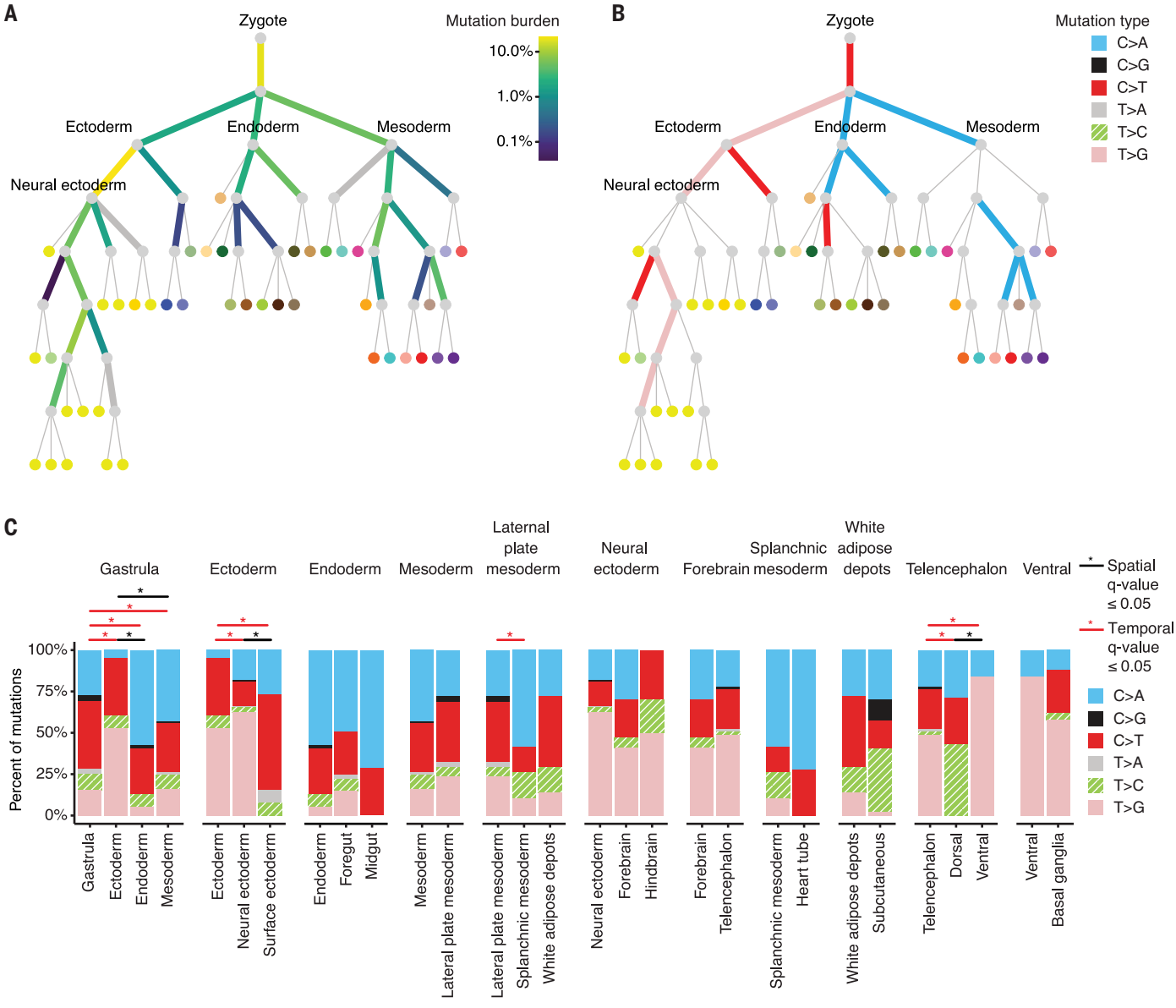

Fig. 2. Mutation burden and spectra of prenatal PZMs across time and space. (**A**) Prenatal PZM mutation burden. Edge color represents the percent of prenatal PZMs mapped to that period in development. Thick gray edges are edges with limited mutation detection power. (**B**) Edge color represents the predominant mutation type of mutations mapped to that edge, as established by binomial testing. Thin gray edges are edges with no predominant mutation type. See fig. S13A for the full set of vertex labels. Adult tissues (leaves of tree) are colored using the GTEx coloring convention (see table S8 for a complete legend). (**C**) Local variation in mutation spectra across developmental space and time. Each facet represents the mutation spectra observed in a parent edge (leftmost bar plot) and its children's edges. Statistically significant differences in mutation spectra are annotated with asterisks.

embryogenesis (*14*, *23*). Notably, the edge mutation burdens were not explained by differential edge mapping power across the developmental tissue tree (*16*) (fig. S17). It is also important to note that these are estimates for mutations that are detectable in adulthood—the data do not allow for extrapolating to all developmentally acquired mutations because some fraction is likely lost through cell death, revertant mosaicism, etc.

We next investigated whether the mutational processes, as proxied by their mutation spectra, varied over development, using binomial tests to establish the predominant mutation type on each edge. There was a strong dichotomy between ectoderm lineages, which tended to have T > G mutations, and endoderm and mesoderm lineages, which tended to have C > A mutations (Fig. 2B). These observations could not be attributed to differences in sample processing (*16*) (fig. S10).

In addition to global changes in mutation across the tree, we also examined local changes by comparing mutation spectra between sibling edges (local spatial differences) and parent-child edges (local temporal differences) (Fig. 2C). Significant spatial and temporal variation was detected during gastrulation and in ectodermal lineages ($Q < 0.05$, multinomial goodness-of-fit test). Differences in mutation spectra across developmental space [$n = 4/8$ (50%) sibling edge comparisons] occurred at similar rates as differences along developmental time [$n = 8/18$ (44%) parent-child comparisons] ($P = 1.00$, Fisher's exact test).

Together, these results suggest that the mutational mechanisms that operate during development may vary across space and time. Although published data are limited, others have also detected variations in mutation spectra in fetal stem cells in humans (*24*) and during early embryogenesis and gametogenesis in mice (*25*). We repeated these analyses using a simplified germ layer tree and observed similar results as from the full developmental tissue tree (fig. S18), which suggests that the development tree definition does not substantially affect the results.

The functional consequences of PZMs across the human life span

The GTEx PZM atlas provides a great opportunity to compare the quality and fitness consequences of mutations that arise at different stages of the human life cycle. First, we annotated the PZM atlas with Combined Annotation Dependent Depletion (CADD), a widely used machine learning classifier of genetic variation (*26*). The CADD score of a genetic variant is a quantitative prediction of deleteriousness, measured on an evolutionary time scale. A mutation was defined as deleterious if the PHRED-scaled CADD score was ≥20. We performed a series of systematic comparisons of PZM CADD scores to identify differences across mutation VAF, developmental time, developmental location, and tissue type.

When comparing prenatal and postnatal PZMs, we found a major effect of VAF on the distribution of CADD scores (Fig. 3A and fig. S19). For prenatal PZMs, low-VAF PZMs were much more deleterious than high-VAF PZMs (odds ratio = 1.9, $P = 2.6 \times 10^{-7}$, Fisher's exact test), whereas no such difference was observed for postnatal PZMs ($P = 0.24$, Wald test). Furthermore, we found that for low-VAF PZMs, deleteriousness decreased over time (odds ratio = 0.58, $P = 1.4 \times 10^{-9}$) but remained constant for high-VAF PZMs ($P = 0.15$). These results suggest that mutations that appear deleterious on an evolutionary time scale may be benign or even beneficial to a growing fetus so long as the mutation remains in a small fraction of cells.

Next, we explored whether deleteriousness varied across the adult human body by comparing postnatal PZMs in each adult tissue. PZM deleteriousness was similar across tissues; however, there were a few exceptions (Fig. 3B). PZMs in 6/48 (13%) tissues were significantly less deleterious than the average tissue, and PZMs in 3/48 (6%) tissues were more deleterious ($Q < 0.05$, Wald test). When analyzed together, the PZMs from all brain regions were also more deleterious than average ($P = 0.02$, Fisher's exact test).

Finally, to provide context for our results, we compared the deleteriousness of GTEx PZMs with other classes of single-nucleotide genetic variation: (i) random mutations (simulated from two different models of neutral evolution), (ii) standing germline variation [from gnomAD, a comprehensive database of germline genetic variation (*27*)], (iii) inherited de novo mutations from cases of disease and controls [from denovo-db, a curated database of de novo mutations (*28*)], and (iv) somatic mutations observed in cancer (from TCGA, a comprehensive database of cancer somatic mutations) (*29*).

The low-VAF prenatal PZMs were the most deleterious class of genetic variation investigated (Fig. 3C and fig. S19). Using the simulated random mutations as a reference, we found postnatal PZMs, de novo mutations in cases, and somatic cancer mutations to be significantly enriched for deleterious mutations ($Q < 0.05$, Fisher's exact test). De novo mutations in controls and high-VAF prenatal PZMs were not statistically different from simulated random mutations. Inherited germline variants were depleted of deleterious mutations, with the extent of depletion increasing with population frequency. These observations were recapitulated in three validation datasets that used a variety of nucleic acid sources and variant-calling methods (*16*) (figs. S20 to S23 and table S13).

The selective constraint on the transcribed exome varies throughout the human life span

The deleteriousness results suggest that selection pressure may be different across classes of genetic variation. We investigated this hypothesis by estimating the selection pressure on PZMs and other classes of genetic variation using dN/dS, a normalized rate of nonsynonymous to synonymous mutations (*30*). dN/dS values >1 were interpreted as evidence for positive selection, whereas negative selection can lead to dN/dS values <1. Using dNdScv, a method for the study of somatic evolution (*11*), we assessed dN/dS across VAF, developmental time, developmental location, and tissue type and contextualized the results by comparing selection pressures on PZMs with other classes of genetic variation as before (*16*) (Fig. 3, D and E, and figs. S24 to S26).

For most tissues of the body, single-tissue dN/dS was not significantly different from 1, consistent with previous work (*11*). However, for postnatal missense mutations, dN/dS was higher for high-VAF PZMs compared with low-VAF PZMs for all tissues en masse and for three tissues or cell types individually [whole blood, Epstein-Barr virus (EBV)–transformed lymphocytes, and adrenal gland] (fig. S24). Additionally, dN/dS estimates for high-VAF postnatal PZMs were higher in cancer driver genes than noncancer driver genes for all tissues en masse, sun-exposed skin, and esophagus mucosa—tissues where the action of adaptive evolution has already been documented (*7*, *31*) (Fig. 3D). These observations are consistent with the expectation that positive selection on a mutation may result in clonal growth, and we detected mutations associated with clonal hematopoiesis of indeterminant potential (CHIP) in the blood of individuals without apparent hematological malignancies (*16*) (fig. S27). Six separate CHIP mutations were detected in seven samples (table S14). Two of the mutations (IDH2 R140Q and MYD88 L273P) are in the 99.99th percentile of recurrent mutations in hematopoietic and lymphoid cancers and have been shown to have gain-of-function properties (*32*, *33*). In total, 0.1% (1/746) of whole-blood donors and 3.5% (6/174) of EBV-transformed lymphocyte donors had a CHIP mutation. Notably, none of the CHIP-positive donors had a history of cancer. The observed CHIP prevalence in GTEx is similar to what we would expect given the age demographics of the cohort and published prevalence rates (*2*).

dN/dS for the low-VAF prenatal PZM class was nominally greater than 1 (missense dN/dS = 1.25, $P = 0.047$) (Fig. 3E). The high-VAF postnatal nonsense mutations showed dN/dS values much less than 1, which can be attributed to sampling bias against transcripts carrying premature stop codons, because of nonsense-mediated decay (*34*). Altogether, the deleteriousness and selection results suggest a dichotomy

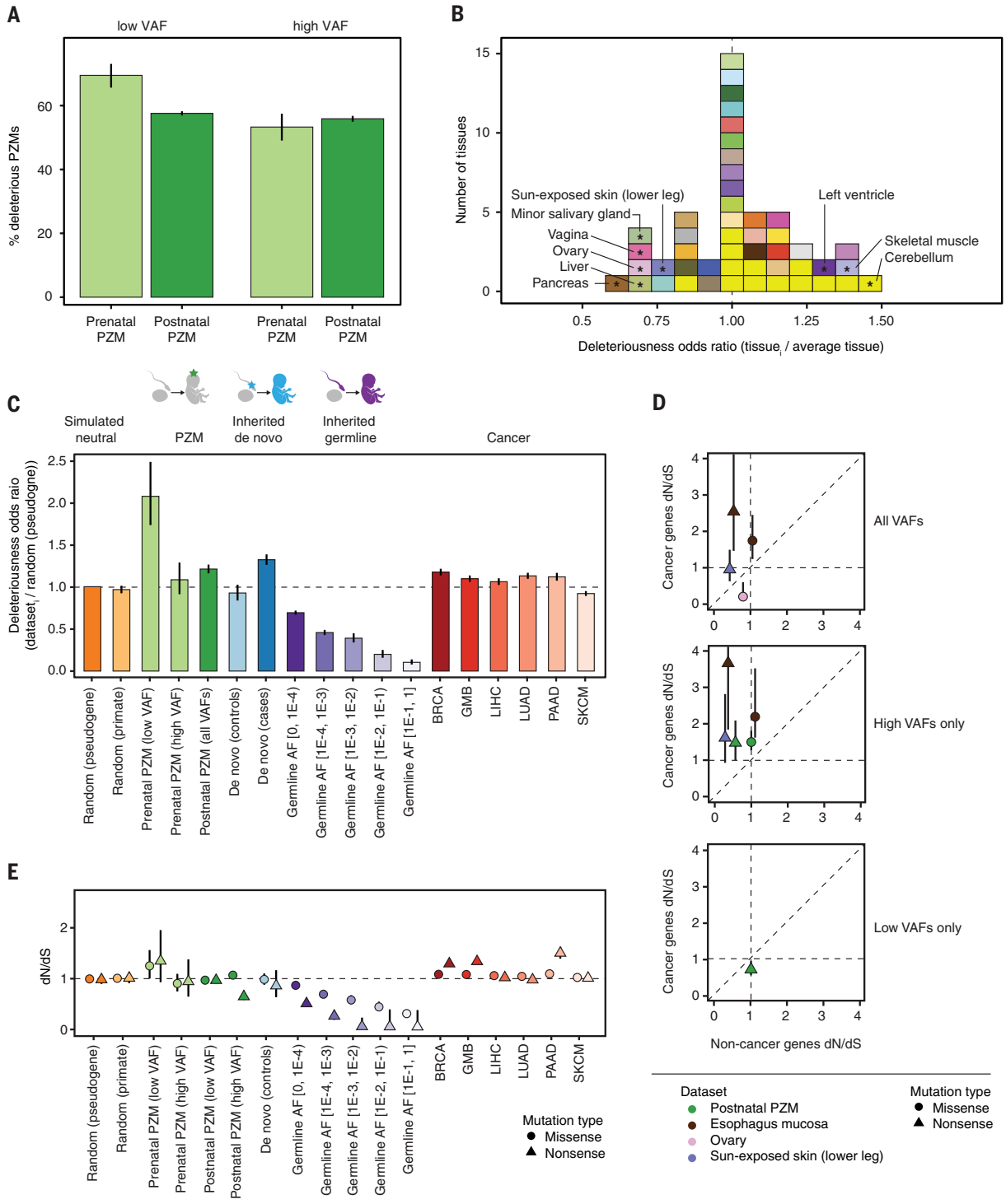

Fig. 3. Deleteriousness and selective pressure changes as a function of VAF, space, time, and classes of genetic variation. (**A**) Relative odds of detecting deleterious mutations across developmental time (gray bars) and VAF bins (green bars). (**B**) Histogram of the odds of detecting deleterious postnatal PZMs in each tissue compared with the average tissue. Tissues are colored using the GTEx coloring convention (see table S8 for a complete legend). Tissues with significant odds ratios (at $Q \leq 0.05$) are marked with asterisks and labeled with their names. The vertical dashed line at odds ratio = 1 indicates no difference in odds. (**C**) Relative odds of detecting deleterious PZM mutations compared with different classes of genetic variation. Dashed line at odds ratio = 1 indicates no difference in odds of detecting deleterious mutations compared with reference group. Error bars represent 95% CIs. (**D**) Comparison of postnatal PZM selection pressure in cancer and noncancer genes. For clarity, only PZM datasets that had different selection pressure between cancer and noncancer genes are shown. (Top) PZM datasets that had variable selection when using all mutations. (Middle) High-VAF mutations. (Bottom) Low-VAF mutations. Error bars represent 95% CIs. Some CIs are smaller than the data point so are not directly visible. (**E**) dN/dS values for classes of genetic variation, as in (C). CIs are plotted behind each data point and are sometimes smaller than the data point size. dN/dS = 1 indicates neutral expectation. AF, allele frequency; BRCA, breast invasive carcinoma; GBM, glioblastoma multiforme; LIHC, liver hepatocellular carcinoma; PAAD, pancreatic adenocarcinoma; SKCM, skin cutaneous melanoma.

between growth within an individual versus growth within a population: Mutations that are selected for within parts of an individual may be detrimental when considered across the entire life span.

Characterization of germ cell PZMs

Construction of a catalog of germ cell PZMs throughout the germ cell life cycle

Although a great deal is known about germline variation (*27*) and de novo mutations (*25*, *35*–*39*), much less is known about the PZMs that seed these forms of inherited genetic variation. To better understand PZMs in germ cells, we characterized and contrasted the mutation burden, spectra, and deleteriousness of germ cell PZMs across the germ cell life cycle.

Because of cell composition differences between male and female gonads, PZMs in testes samples could be confidently mapped to germ cells, but PZMs in ovary samples could not (*16*) (fig. S28 and table S15). Therefore, only testicular germ cell PZMs were analyzed further. Germ cell PZMs were classified into gonosomal (present in somatic and germ cells) and germ cell–specific. In total, 571 germ cell PZMs were identified in the bulk testis from 281 testis donors, of which 12% were putative gonosomal PZMs and the remaining 88% were putative germ cell–specific PZMs. As expected, germ cell–specific PZM burden was positively associated with donor age ($P = 0.03$), but gonosomal mutation burden was not ($P = 0.28$). Additionally, as expected, germ cell–specific PZMs had lower VAFs than gonosomal PZMs ($P = 1.3 \times 10^{-14}$, Mann-Whitney U test; fig. S28E).

Testicular germ cell PZMs represent the full reservoir of mutations that can be passed on to progeny. We hypothesized that the selection pressures on spermatogenesis, fertilization, and prenatal development may alter the types of mutations that pass through each of these bottlenecks of life. To examine germ cell PZMs that passed the spermatogenesis bottleneck, we generated whole-exome sequencing data on small, 200-cell pools of ejaculated sperm and identified and validated 83 PZMs in the same genomic regions that we assessed in the GTEx RNA-seq samples (defined as the allowable transcriptome) (*16*) (tables S1 and S16 and fig. S29). To examine germ cell PZMs that completed prenatal development, we used ~17,000 de novo mutations in the allowable transcriptome from denovo-db (*28*).

The mutation spectra for each germ cell mutation dataset were statistically different from the others (Fig. 4A and table S17; chi-square test). Although C > T was the most common mutation type in all datasets, C > A was the most variable. Hierarchical clustering of the spectra nested the classes in developmental order, indicating that the mutation spectra shift during development (Fig. 4A, inset). Given the complex ascertainment of these diverse mutation call-sets, we cannot exclude the possibility that some of the apparent structure is attributable to differences in mutation detection among sources, as a result of either bioinformatic or experimental effects.

Deleterious mutations are likely purged during the germ cell life cycle

Consistent with the action of purifying selection on male germ cells, we found that mutation deleteriousness decreased over the germ cell life cycle when comparing testicular germ cell PZMs and de novo mutations in controls (Fig. 4B). By contrast, de novo mutations from cases of disease were just as likely to be deleterious as testis PZMs. To replicate these observations, we performed a similar analysis using only DNA-based measurements from published datasets (*10*, *16*, *40*) (fig. S30). Both the fraction of coding mutations and the odds of detecting a deleterious mutation decreased over the germ cell life cycle in the independent datasets (fig. S30). Donor age was not associated with PZM deleteriousness in each dataset.

The mutation rate during male gametogenesis is dynamic

We estimated the mutation rate (the number of mutations in the transcriptome per cell division) for each of three major stages during male gametogenesis (*16*). Consistent with previous work (*37*), the observed mutation rate was higher in prenatal time points than the postnatal time point (Fig. 4C). The observed lower mutation rate during adulthood may be a strategy to limit the number of deleterious mutations that are passed to the next generation. Unlike Rahbari *et al.* (*37*) and other studies that have used transmitted de novo mutations to measure mutation rates (*35*, *36*, *38*, *39*), these estimates reflect mutation rates in germ cells in the testis and thus offer insight on germ cell mutagenesis.

Blood is a poor surrogate for measuring mosaicism of gonosomal PZMs

Motivated by the fact that only a small subset of tissue types is easily and ethically accessible in antemortem human subjects research, we hypothesized that more-accessible tissues may be useful surrogates for examining prenatal PZMs in less-accessible tissues. The results of such analyses may shed light on the cellular dynamics of human development and implications for preconception genetic counseling and de novo mutation discovery.

We fit a mixed-effects model to predict whether a gonosomal PZM was detected in a somatic tissue while controlling for technical effects (*16*). Unexpectedly, 88% (38/43) of tissues had significantly higher odds of detecting gonosomal PZMs than in blood (Fig. 4D), which suggests that blood is a poor surrogate for detecting gonosomal PZMs. Additionally, 76% (32/42) of somatic tissues had a significant linear correlation between the somatic VAF and the germ cell VAF (Fig. 4, E and F; $Q < 0.05$, Pearson's correlation test), which suggests that somatic tissues may offer a faithful representation of gonosomal PZMs in germ cells. These observations were not an artificial result of germline variant filtering or our cross-sample mutation-calling strategy (*16*) (fig. S31). Although 82% of GTEx donors were genotyped using blood, for 6% of GTEx donors, a nonblood tissue was used for genotyping, and for 12% of donors, no genotyping data were available. There was no detectable difference among these three groups in the probability of detecting a prenatal PZM in blood while controlling for other confounders; this suggests that poor detection of gonosomal PZMs in blood is not simply the result of aggressive germline filtering using genotype calls from blood-derived DNA (*16*).

Discussion

In this work, we present one of the most comprehensive and diverse surveys of PZM variation in normal individuals, which should prove a valuable resource for understanding the causes and consequences of PZMs across the body. By linking these mutation calls to the vast data and tissue resources of the GTEx project, there are a number of analyses that could be attempted. First, if there is a heritable component to PZM burden, variants modulating this burden may be detectable using genome-wide association studies (GWASs) (*41*, *42*). Second, the impact of PZMs on gene expression traits, both in cis and trans, can be directly assessed (*9*, *43*). Third, the spatial and cell-type distribution of the mutations reported here could be mapped in banked tissue samples from the GTEx donors (*7*, *44*), and the mutation type and burden of each sample could be associated with histology images collected by the GTEx project. We performed extensive validation of our PZM call-set, and these validation data will be helpful in training algorithms for PZM detection.

We observed a number of notable features regarding the developmental origins of mutations that deserve follow up. Most intriguing is a class of low-VAF prenatal mutations that appear to have the highest fraction of deleterious mutations across the human life span, even considering disease states. This observation, based on a definition of deleteriousness on an evolutionary time scale, suggests that the functional consequences of mutation can have opposite fitness effects at different stages of the life cycle of genomes and in different cellular contexts. One well-established example of marked differences in fitness effects between somatic and germline cells is the RAS-MAPK pathway, in which gain-of-function mutations provide a

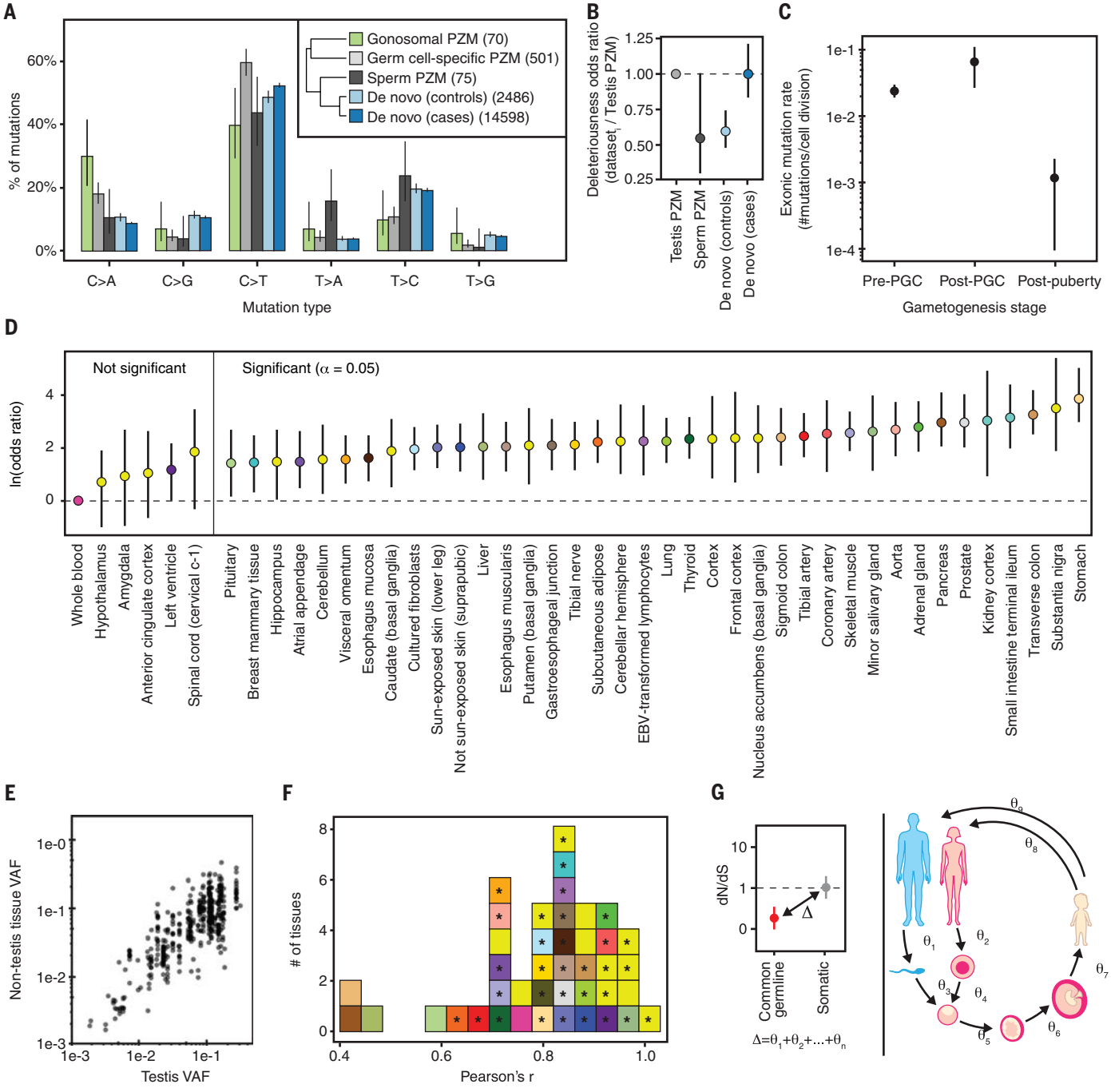

Fig. 4. Germ cell PZM characteristics. (**A**) Mutation spectra of different germ cell mutation classes. Number of mutations used in each dataset is listed in the inset. (Inset) Hierarchical clustering of germ cell mutation spectra. (**B**) Relative odds of detecting deleterious mutations across germ cell datasets compared with testis PZMs. Bars are colored by dataset. Horizontal black line at odds ratio = 1 denotes no difference in odds. (**C**) Germ cell mutation rate varies during gametogenesis in males. (**D**) Most somatic tissues have a higher odds of detecting a gonosomal PZM than blood. Natural log odds ratio for detecting a gonosomal PZM in each somatic tissue compared with blood. Dashed line at Y = 0 denotes no difference in odds. (**E**) Comparison of gonosomal PZM VAF in nontestis tissues versus testis tissue. (**F**) Distribution of tissue-specific Pearson correlations of $\log_{10}$-transformed gonosomal PZM VAFs in each somatic tissue and testis. Significant correlations at $Q \leq 0.05$ are marked with asterisks. (**G**) Schematic of the difference in selective constraint between germline and somatic genetic variation partitioned into discrete stages of the life cycle. [(A), (B), (C), and (D)] Error bars denote 95% CIs.

transmission advantage to male germ cells but are often reproductively lethal for the resulting conceptus (*45*, *46*). Although some parallels have been noted between molecular mechanisms of carcinogenesis and normal embryogenesis (*47*, *48*), there are essentially no data on the potential adaptive effects of PZMs on embryonic or fetal development in healthy individuals.

We advise caution in the interpretation of the dN/dS values for multitissue PZMs. Although we have evaluated obvious sources of technical error, such as the multitissue ascertainment (fig. S25) and small sample size (fig. S26), there may be other complexities influencing this rather general statistic, including recurrent mutation

and changes in mutation processes throughout development. Clearly it will be important to continue research into appropriate statistical methods for assessing fitness consequences of PZMs from multitissue datasets.

We found that blood-derived RNA appeared to be a poor proxy for detection of gonosomal mutations. On the basis of these results, for trio studies, we recommend that sperm (a direct readout of germ cells) should be profiled in males and skin (which is predicted to be more than five times as likely as blood to contain a gonosomal PZM) should be profiled in females. It should be noted that these findings on gonosomal PZMs were based on analysis of data exclusively from male tissues. We are optimistic that this conclusion will hold for female gonosomal mutations. In humans, male and female germ cells are both formed from a common progenitor cell type, primordial germ cells (PGCs). Early embryonic development, up to and including the formation of PGCs, is the time frame in which gonosomal mutations occur and is thought to occur identically in males and females (*49*). The developmental phylogeny that relates PGCs and the three germ layers is unclear, and the patterns of gonosomal mutations observed across human tissues may yield important insight into the matter. Some studies have indicated that PGCs may be most related to the mesoderm: Incipient mesoderm or mesendoderm cells can be induced to form PGC-like cells in vitro (*50*, *51*), and PGCs may share expression markers with mesoderm or primitive streak (*52*). However, loss of BLIMP1, a key driver of germline identity, from germline-competent cells leads to activation of a default neuronal differentiation program (*50*). When mapping gonosomal mutations frequencies across the body, we found that brain tissues were most similar to the testis (Fig. 4F). This might be an indication that PGCs and the ectoderm share a closer developmental origin.

We reported a large difference in deleteriousness and dN/dS inferred from PZMs and inherited germline variants, consistent with strong purifying selection reducing the transmission of deleterious mutation across generations. An important future direction is to dissect and quantify the physiological basis of this purifying selection (Fig. 4G). With careful thought and experimental design, it should be possible to model the steps of the human life cycle where purifying selection can occur, to estimate the strength of selection at each step, and to translate these data into life stage–specific measures of selective constraint for each gene in the genome. This would be of great benefit to human geneticists, who rely heavily on selective-constraint measures aggregated across the life cycle (such as CADD) for interpretation of genetic variants in the context of disease (*53*, *54*). Stage-specific constraint metrics could augment current methods for variant interpretation to be more relevant to the tissue and developmental time affected by a disease.

Materials and methods summary

GTEx data

We detected PZMs in the GTEx v8 dataset. To achieve a high-quality dataset, we removed RNA-seq samples that had an RNA integrity number (RIN) < 6, were derived from tissues with overall poor quality (*8*), or had an extremely high PZM mutation burden (table S2). We also confirmed that none of the analyzed samples were from transplanted tissue. After our quality control, there were 14,672 samples from 944 donors from 48 diverse tissue and cell types. Library preparation, sequencing, alignment, and GTEx quality control are described in detail in Aguet *et al.* (*15*).

Algorithms for detecting PZMs

LachesisDetect contains four basic steps. First, alignment files are filtered for extremely high-quality alignments. Next, the algorithm leverages cohort-wide information by simultaneously analyzing all samples to estimate position-specific error models for >115 Mb of the transcriptome. LachesisDetect uses these models to detect putative PZMs with single-sample calling. Third, the method removes sources of false-positive PZMs, such as RNA editing and allele-specific expression of germline variants, using >15 filters based on theoretical and experimental validation metrics. In the last step, the method leverages donor information by jointly analyzing all samples in a donor to detect mutations with low power and estimate empirical false-positive rates (fig. S1).

PZM validation

We performed several orthogonal validation experiments to quantify the FDR of the mutation-calling algorithm. These efforts included both in silico and experimental approaches and involved analysis of both DNA and RNA from the tissues used for mutation detection. A summary of the validation results is provided in table S3. We analyzed independent genomics datasets generated by the ENCODE project on four GTEx donors, encompassing 245 DNA assays and 67 RNA assays generated from four GTEx donors. Finally, we generated our own validation data by performing targeted DNA-seq of >1650 putative PZMs using DNA from GTEx donors.

Mutation burden modeling

To evaluate biological and technical sources of variation in mutation burden, we used linear mixed-effect models. We explored a large variety of model choices to arrive at our final modeling framework, comparing modeling choices using deviance, stability of model fitting, and other diagnostics. We used type II ANOVA to summarize the relative contributions of covariates.

Algorithm for mapping PZMs to a developmental tree

We manually derived two developmental tissue trees that represent the phylogenetic relationships among GTEx tissues during human development using information from the literature—the full tree and the simplified germ layer tree. We then developed an algorithm, LachesisMap, to reconstruct the phylogenetic history of multitissue PZMs. The algorithm jointly analyzes all multitissue PZMs and accounts for missing data as well as differential PZM detection power resulting from differences in VAF, expression level, and tissue profiling in the dataset.

Sperm sequencing experiments

Ejaculated sperm and venous blood were collected from a European American. Sperm samples had normal sperm density, sperm motility, and morphology. Fresh ejaculates were stained using the LIVE/DEAD Sperm Viability Kit (Invitrogen) and propidium iodide (PI). Sperm samples were then selectively sorted using fluorescence-activated cell sorting (FACS) into 96 well plates (~200 sperm cells per well) and 5-ml Falcon tubes based on their staining. We used MALBAC amplification (*55*) to prepare up to 1.5 μg of DNA from each pool of sperm using a kit, and six pools were selected for sequencing. Exome library preparation was performed according to the manufacturer's protocol using 50 ng of preamplified MALBAC reactions or DNA extracted from blood.

REFERENCES AND NOTES

1. D. Melzer, L. C. Pilling, L. Ferrucci, The genetics of human ageing. *Nat. Rev. Genet.* **21**, 88–101 (2020). doi: 10.1038/s41576-019-0183-6; pmid: 31690828
2. G. Genovese *et al.*, Clonal hematopoiesis and blood-cancer risk inferred from blood DNA sequence. *N. Engl. J. Med.* **371**, 2477–2487 (2014). doi: 10.1056/NEJMoa1409405; pmid: 25426838
3. M. Xie *et al.*, Age-related mutations associated with clonal hematopoietic expansion and malignancies. *Nat. Med.* **20**, 1472–1478 (2014). doi: 10.1038/nm.3733; pmid: 25326804
4. A. L. Young, G. A. Challen, B. M. Birmann, T. E. Druley, Clonal haematopoiesis harbouring AML-associated mutations is ubiquitous in healthy adults. *Nat. Commun.* **7**, 12484 (2016). doi: 10.1038/ncomms12484; pmid: 27546487
5. M. A. Lodato *et al.*, Somatic mutation in single human neurons tracks developmental and transcriptional history. *Science* **350**, 94–98 (2015). doi: 10.1126/science.aab1785; pmid: 26430121
6. A. Abyzov *et al.*, One thousand somatic SNVs per skin fibroblast cell set baseline of mosaic mutational load with patterns that suggest proliferative origin. *Genome Res.* **27**, 512–523 (2017). doi: 10.1101/gr.215517.116; pmid: 28235832
7. I. Martincorena *et al.*, High burden and pervasive positive selection of somatic mutations in normal human skin. *Science* **348**, 880–886 (2015). doi: 10.1126/science.aaa6806; pmid: 25999502
8. K. Yizhak *et al.*, RNA sequence analysis reveals macroscopic somatic clonal expansion across normal tissues. *Science* **364**, eaaw0726 (2019). doi: 10.1126/science.aaw0726; pmid: 31171663
9. P. E. García-Nieto, A. J. Morrison, H. B. Fraser, The somatic mutation landscape of the human body. *Genome Biol.* **20**, 298 (2019). doi: 10.1186/s13059-019-1919-5; pmid: 31874648

10. L. Moore *et al*., The mutational landscape of human somatic and germline cells. *Nature* **597**, 381–386 (2021). doi: 10.1038/s41586-021-03822-7; pmid: 34433962
11. I. Martincorena *et al*., Universal patterns of selection in cancer and somatic tissues. *Cell* **171**, 1029–1041.e21 (2017). doi: 10.1016/j.cell.2018.06.001; pmid: 29906452
12. T. N. Wong *et al*., Role of *TP53* mutations in the origin and evolution of therapy-related acute myeloid leukaemia. *Nature* **518**, 552–555 (2015). doi: 10.1038/nature13968; pmid: 25487151
13. X. Chen *et al*., Non-invasive early detection of cancer four years before conventional diagnosis using a blood test. *Nat. Commun.* **11**, 3475 (2020). doi: 10.1038/s41467-020-17316-z; pmid: 32694610
14. T. H. H. Coorens *et al*., Extensive phylogenies of human development inferred from somatic mutations. *Nature* **597**, 387–392 (2021). doi: 10.1038/s41586-021-03790-y; pmid: 34433963
15. F. Aguet *et al*., The GTEx Consortium atlas of genetic regulatory effects across human tissues. bioRxiv 787903 [Preprint] (2019). https://doi.org/10.1101/787903
16. See the supplementary materials.
17. M. Enge *et al*., Single-cell analysis of human pancreas reveals transcriptional signatures of aging and somatic mutation patterns. *Cell* **171**, 321–330.e14 (2017). doi: 10.1016/j.cell.2017.09.004; pmid: 28965763
18. US Cancer Statistics Working Group, US Cancer Statistics Data Visualizations Tool (Centers for Disease Control and Prevention, 2021); https://www.cdc.gov/cancer/dataviz.
19. J. M. Goldmann *et al*., Differences in the number of de novo mutations between individuals are due to small family-specific effects and stochasticity. *Genome Res.* **31**, 1513–1518 (2021). doi: 10.1101/gr.271809.120; pmid: 34301630
20. S. A. Frank, Somatic evolutionary genomics: Mutations during development cause highly variable genetic mosaicism with risk of cancer and neurodegeneration. *Proc. Natl. Acad. Sci. U.S.A.* **107**, 1725–1730 (2010). doi: 10.1073/pnas.0909343106; pmid: 19805033
21. M. D. Lynch *et al*., Spatial constraints govern competition of mutant clones in human epidermis. *Nat. Commun.* **8**, 1119 (2017). doi: 10.1038/s41467-017-00993-8; pmid: 29066762
22. L. B. Alexandrov *et al*., The repertoire of mutational signatures in human cancer. *Nature* **578**, 94–101 (2020). doi: 10.1038/s41586-020-1943-3; pmid: 32025018
23. J.-J. Gao *et al*., Highly variable recessive lethal or nearly lethal mutation rates during germ-line development of male *Drosophila melanogaster*. *Proc. Natl. Acad. Sci. U.S.A.* **108**, 15914–15919 (2011). doi: 10.1073/pnas.1100233108; pmid: 21890796
24. E. Kuijk *et al*., Early divergence of mutational processes in human fetal tissues. *Sci. Adv.* **5**, eaaw1271 (2019). doi: 10.1126/sciadv.aaw1271; pmid: 31149636
25. S. J. Lindsay, R. Rahbari, J. Kaplanis, T. Keane, M. E. Hurles, Similarities and differences in patterns of germline mutation between mice and humans. *Nat. Commun.* **10**, 4053 (2019). doi: 10.1038/s41467-019-12023-w; pmid: 31492841
26. M. Kircher *et al*., A general framework for estimating the relative pathogenicity of human genetic variants. *Nat. Genet.* **46**, 310–315 (2014). doi: 10.1038/ng.2892; pmid: 24487276
27. K. J. Karczewski *et al*., The mutational constraint spectrum quantified from variation in 141,456 humans. *Nature* **581**, 434–443 (2020). doi: 10.1038/s41586-020-2308-7; pmid: 32461654
28. T. N. Turner *et al*., denovo-db: A compendium of human *de novo* variants. *Nucleic Acids Res.* **45**, D804–D811 (2017). doi: 10.1093/nar/gkw865; pmid: 27907889
29. ICGC/TCGA Pan-Cancer Analysis of Whole Genomes Consortium, Pan-cancer analysis of whole genomes. *Nature* **578**, 82–93 (2020). doi: 10.1038/s41586-020-1969-6; pmid: 32025007
30. N. Goldman, Z. Yang, A codon-based model of nucleotide substitution for protein-coding DNA sequences. *Mol. Biol. Evol.* **11**, 725–736 (1994). doi: 10.1093/oxfordjournals.molbev.a040153; pmid: 7968486
31. I. Martincorena *et al*., Somatic mutant clones colonize the human esophagus with age. *Science* **362**, 911–917 (2018). doi: 10.1126/science.aau3879; pmid: 30337457
32. P. S. Ward *et al*., The common feature of leukemia-associated IDH1 and IDH2 mutations is a neomorphic enzyme activity converting α-ketoglutarate to 2-hydroxyglutarate. *Cancer Cell* **17**, 225–234 (2010). doi: 10.1016/j.ccr.2010.01.020; pmid: 20171147
33. V. N. Ngo *et al*., Oncogenically active *MYD88* mutations in human lymphoma. *Nature* **470**, 115–119 (2011). doi: 10.1038/nature09671; pmid: 21179087
34. M. A. Rivas *et al*., Effect of predicted protein-truncating genetic variants on the human transcriptome. *Science* **348**, 666–669 (2015). doi: 10.1126/science.1261877; pmid: 25954003
35. 1000 Genomes Project, Variation in genome-wide mutation rates within and between human families. *Nat. Genet.* **43**, 712–714 (2011). doi: 10.1038/ng.862; pmid: 21666693
36. J. C. Roach *et al*., Analysis of genetic inheritance in a family quartet by whole-genome sequencing. *Science* **328**, 636–639 (2010). doi: 10.1126/science.1186802; pmid: 20220176
37. R. Rahbari *et al*., Timing, rates and spectra of human germline mutation. *Nat. Genet.* **48**, 126–133 (2016). doi: 10.1038/ng.3469; pmid: 26656846
38. A. Kong *et al*., Rate of de novo mutations and the importance of father's age to disease risk. *Nature* **488**, 471–475 (2012). doi: 10.1038/nature11396; pmid: 22914163
39. J. J. Michaelson *et al*., Whole-genome sequencing in autism identifies hot spots for de novo germline mutation. *Cell* **151**, 1431–1442 (2012). doi: 10.1016/j.cell.2012.11.019; pmid: 23260136
40. X. Yang *et al*., Developmental and temporal characteristics of clonal sperm mosaicism. *Cell* **184**, 4772–4783.e15 (2021). doi: 10.1016/j.cell.2021.07.024; pmid: 34388390
41. A. Hodgkinson *et al*., High-resolution genomic analysis of human mitochondrial RNA sequence variation. *Science* **344**, 413–415 (2014). doi: 10.1126/science.1251110; pmid: 24763589
42. P.-R. Loh *et al*., Insights into clonal haematopoiesis from 8,342 mosaic chromosomal alterations. *Nature* **559**, 350–355 (2018). doi: 10.1038/s41586-018-0321-x; pmid: 29995854
43. J. Ding *et al*., Systematic analysis of somatic mutations impacting gene expression in 12 tumour types. *Nat. Commun.* **6**, 8554 (2015). doi: 10.1038/ncomms9554; pmid: 26436532
44. A. Erickson *et al*., Spatially resolved clonal copy number alterations in benign and malignant tissue. *Nature* **608**, 360–367 (2022). doi: 10.1038/s41586-022-05023-2; pmid: 35948708
45. G. J. Maher *et al*., Selfish mutations dysregulating RAS-MAPK signaling are pervasive in aged human testes. *Genome Res.* **28**, 1779–1790 (2018). doi: 10.1101/gr.239186.118; pmid: 30355600
46. A. Goriely, A. O. M. Wilkie, Paternal age effect mutations and selfish spermatogonial selection: Causes and consequences for human disease. *Am. J. Hum. Genet.* **90**, 175–200 (2012). doi: 10.1016/j.ajhg.2011.12.017; pmid: 22325359
47. N. M. Aiello, B. Z. Stanger, Echoes of the embryo: Using the developmental biology toolkit to study cancer. *Dis. Model. Mech.* **9**, 105–114 (2016). doi: 10.1242/dmm.023184; pmid: 26839398
48. T. Gong *et al*., A time-resolved multi-omic atlas of the developing mouse liver. *Genome Res.* **30**, 263–275 (2020). doi: 10.1101/gr.253328.119; pmid: 32051188
49. Y.-T. Lin, B. Capel, Cell fate commitment during mammalian sex determination. *Curr. Opin. Genet. Dev.* **32**, 144–152 (2015). doi: 10.1016/j.gde.2015.03.003; pmid: 25841206
50. K. Sasaki *et al*., Robust in vitro induction of human germ cell fate from pluripotent stem cells. *Cell Stem Cell* **17**, 178–194 (2015). doi: 10.1016/j.stem.2015.06.014; pmid: 26189426
51. T. Kobayashi *et al*., Principles of early human development and germ cell program from conserved model systems. *Nature* **546**, 416–420 (2017). doi: 10.1038/nature22812; pmid: 28607482
52. R. C. V. Tyser *et al*., Single-cell transcriptomic characterization of a gastrulating human embryo. *Nature* **600**, 285–289 (2021). doi: 10.1038/s41586-021-04158-y; pmid: 34789876
53. S. Petrovski, Q. Wang, E. L. Heinzen, A. S. Allen, D. B. Goldstein, Genic intolerance to functional variation and the interpretation of personal genomes. *PLOS Genet.* **9**, e1003709 (2013). doi: 10.1371/journal.pgen.1003709; pmid: 23990802
54. K. Eilbeck, A. Quinlan, M. Yandell, Settling the score: Variant prioritization and Mendelian disease. *Nat. Rev. Genet.* **18**, 599–612 (2017). doi: 10.1038/nrg.2017.52; pmid: 28804138
55. P. G. Engström *et al*., Systematic evaluation of spliced alignment programs for RNA-seq data. *Nat. Methods* **10**, 1185–1191 (2013). doi: 10.1038/nmeth.2722; pmid: 24185836
56. N. Rockweiler, D. Contrad, conradlab/RockweilerEtAl: v0.1.0-alpha, version 0.1.0-alpha, Zenodo (2022); https://doi.org/10.5281/zenodo.7378922.

ACKNOWLEDGMENTS

We thank the GTEx donors and families for their generous and selfless donation of tissues and organs for the advancement of science. We thank T. Lappalainen (New York Genome Center and KTH Royal Institute of Technology), H. Leitch (London Institute of Medical Sciences), G. Coop (UC Davis), I. Martincorena (Sanger Institute), the M. Griffiths laboratory (Washington University), the S. Montgomery laboratory (Stanford University), and the Conrad and Cohen laboratories (Washington University) for data sharing and helpful discussions. Sequencing for the validation experiments was performed by the Genome Technology Access Center (GTAC) in the Department of Genetics at Washington University School of Medicine. We appreciate obtaining access to de novo mutations on SFARI base (https://base.sfari.org). We thank the following funders for their support of the TwinsUK resource: Wellcome Trust, Medical Research Council, European Union, Chronic Disease Research Foundation (CDRF), the National Institute for Health Research (NIHR)–funded BioResource Clinical Research Facility, and the Biomedical Research Centre based at Guy's and St Thomas' NHS Foundation Trust in partnership with King's College London. We also acknowledge that this manuscript includes several analyses that focus on GTEx donors with European and African American ancestry and less so on other ancestries in GTEx. This decision was made so that we would have higher statistical power to detect potentially rare genetic signals that may vary across populations. We hope that in future studies, larger numbers of Black, Indigenous, and People of Color are included so that we can learn about all populations in an equitable manner. **Funding:** This study was supported by National Institutes of Health grants R01MH101810 (to D.F.C.), R01HG007178 (to D.F.C.), and R01HD078641 (to D.F.C.); National Human Genome Research Institute grant T32HG000045 (to B.A.C.); and Medical Research Council grants MR/M004422/1 (to K.S.S.) and MR/R023131/1 (to K.S.S.). **Author contributions:** D.F.C. conceived the study. N.B.R. designed and performed research and analyzed data. W.H.W. and E.Z.T. assisted with experimental design and sample procurement and generated sequencing libraries for validation experiments. M.J.N. and L.N. performed and analyzed data from the sperm experiment. B.M. and A.Z. contributed to analyses. A.R., C.W.D., and N.H. contributed to the study design. K.A.V.-C. contributed to data visualization. D.F.C., K.G.A., and B.A.C. supervised the project. N.B.R. and D.F.C. wrote the manuscript in consultation with all authors. **Competing interests:** D.F.C. is an advisor to Paterna Biosciences. All other authors declare that they have no competing interests. **Data and materials availability:** All GTEx protected data are available through the database of Genotypes and Phenotypes (dbGaP) (accession no. phs000424.v8). Access to the raw sequence data is provided through the AnVIL platform (https://gtexportal.org/home/protectedDataAccess). The cancer results are based on data generated by the TCGA Research Network: https://www.cancer.gov/ccg/research/genome-sequencing/tcga. De novo mutations were obtained from denovo-db (https://denovo-db.gs.washington.edu/denovo-db/). Data generated on GTEx tissues by the ENCODE project are available from https://www.encodeproject.org. Source code used in this study is available from https://github.com/conradlab/RockweilerEtAl. Archived source code at the time of publication is available from Zenodo (*56*).

SUPPLEMENTARY MATERIALS

science.org/doi/10.1126/science.abn7113
Materials and Methods
Figs. S1 to S31
Tables S1 to S17
References (*57*–*123*)
MDAR Reproducibility Checklist

View/request a protocol for this paper from *Bio-protocol*.

Submitted 16 December 2021; accepted 17 March 2023
10.1126/science.abn7113